Supplementary Information (SI) for Journal of Materials Chemistry A.
This journal is © The Royal Society of Chemistry 2026

Supplementary Information

Engineering Cu-Ag Interfaces for Selective Acetate Production in CO_2 Electroreduction

Chayapat Thammaniphit[1], Pongtanawat Khemthong[2], Teera Butburee[2], Jirapat Santatiwongchai[2], Weradesh Sangkhun[2], Kornkamon Meesombad[2], Alexander Gonzalez[3], Tobias Hanrath[3], Pongkarn Chakthranont[2]*, Rungthiwa Methaapanon[1]*

[1]Centre of Excellence in Particle and Material Processing Technology, Department of Chemical Engineering, Faculty of Engineering, Chulalongkorn University, Bangkok, 10330, Thailand

[2]National Nanotechnology Center (NANOTEC), National Science and Technology Development Agency (NSTDA), Pathum Thani, 12120 Thailand

[3]Robert Frederick Smith School of Chemical and Biomolecular Engineering, Cornell University, Ithaca, NY 14853, USA

*E-mail: rungthiwa.m@chula.ac.th, pongkarn.cha@nanotec.or.th

Table of contents

Activity comparison

Table S1 Reported CO_2RR performances of Cu-base catalysts to produce acetate from the literature.

Catalyst	Acetate (%FE)	current density (mA cm^{-2})	Potential (V vs. RHE)	electrolyte	Electrolytic cell	Ref.
Cu_2O-Cu^0	76	0.46	-0.4	0.3M $KHCO_3$	H-cell	[1]
Cu-Cu_2O-2	48	11.5	-0.4	0.1M KCl	H-cell	[2]
PcCu-TFPN	90.3	12.5	-0.8	0.1M $KHCO_3$	Flow cell	[3]
Co-corrole	13	2.9	-0.955	0.1M $NaClCO_4$ with phosphate buffer	H-cell	[4]
NDD/Si RA	77.3	~1	-0.8	0.5M $NaHCO_3$	H-cell	[5]
Cu-CuI	<5	894	-1.0	1M KOH	Flow cell	[6]

Table S2 Reported CO_2RR performances of Cu-Ag catalysts from the literature.

Catalyst	Ag (%mol)	current density (mA cm^{-2})	H_2 (%FE)	CO (%FE)	EtOH (%FE)	C_2H_4 (%FE)	Acetate (%FE)	Potential (V vs. RHE)	electrolyte	Electrolytic cell	Ref.
Ag Core-Cu shell	96.7	320	~10	~10	52.6	27.7	~1	-1	3 M KOH	Flow-cell	[7]
Cu NWs + Ag Particle	95.2	25.1	~20	~18	16.5	14.9	3.4	-1.1	0.1 M $KHCO_3$	H-cell	[8]
Cu-Ag alloy nanorods	54.5	213.3	17	28.9	18.5	24.1	5.3	-1	1 M KOH	Flow-cell	[9]
Cu-Ag tandem	54	320	~11	~15	10.5	13	17	-0.7	1 M KOH	Flow-cell	[10]
Cu-Ag tandem	46.9	2.5	~25	~20	22.5	16.8	2.2	-1.2	0.1 M $KHCO_3$	H-cell	[11]
Cu-Ag alloy	33	40	12	0.8	17	1.5	0	-0.95	0.5 M KHCO3	H-cell	[12]
Atomic Cu-Ag pairs	30	6.6	18	17	13	-	50	-0.5	0.1M $KHCO_3$	H-cell	[13]
Cu-Ag nanowires	18	2.5	12.8	53.21	3.07	19.5	1.15	-1.17	0.1M $KHCO_3$	H-cell	[14]
Cu-Ag alloy	16	5	25	10	15	12	0	-0.9	0.5 M $KHCO_3$	H-cell	[15]
Cu-Ag alloy film	14	250	7	5	40	30	12	-0.67	1 M KOH	Flow-cell	[16]
Cu-Ag tandem	12	-	~20	~30	-	4	0	-1.17	0.1 M$KHCO_3$	H-cell	[17]
Cu-Ag alloy	10	50	~25	~48	7	15	2	-0.85	1 M KOH	Flow-cell	[18]
Cu-Ag Janus	3.48	~35	~18	~7	19.8	~50	0	-1.2	0.1M $KHCO_3$	H-cell	[19]
Ag Core-Cu shell	1.74	300	10	15	23.2	43.9	5.9	-1.6	1M $KHCO_3$	Flow-cell	[20]
Nanoscale Cu–Ag alloy	**60**	**320**	**12.3**	**32.9**	**9.1**	**6**	**31.1**	**-0.6**	**1 M KOH**	**Flow cell**	**This work**

Catalyst synthesis & characterizations

Deposition of Cu, Ag, and Cu-Ag thin films by magnetron sputtering

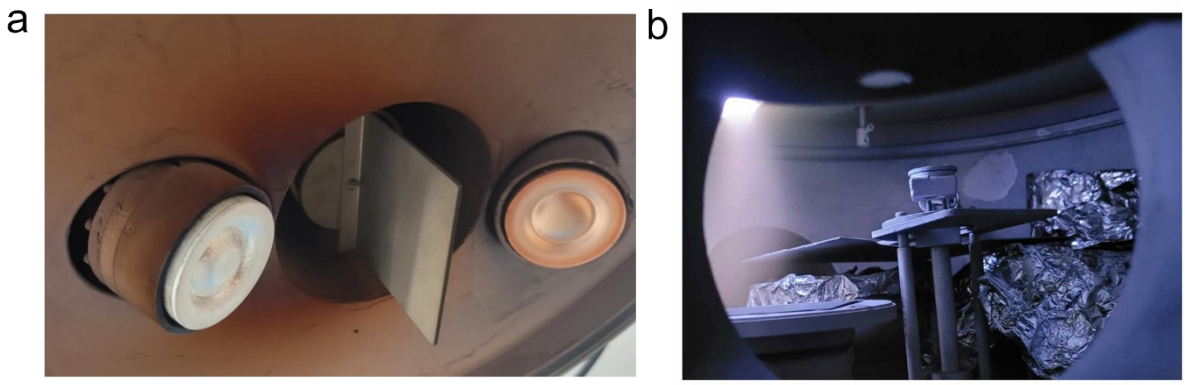

Figure S1 (a) Cu and Ag targets for the co-sputtering method; (b) interior view of the sputtering chamber during deposition, showing the plasma glow.

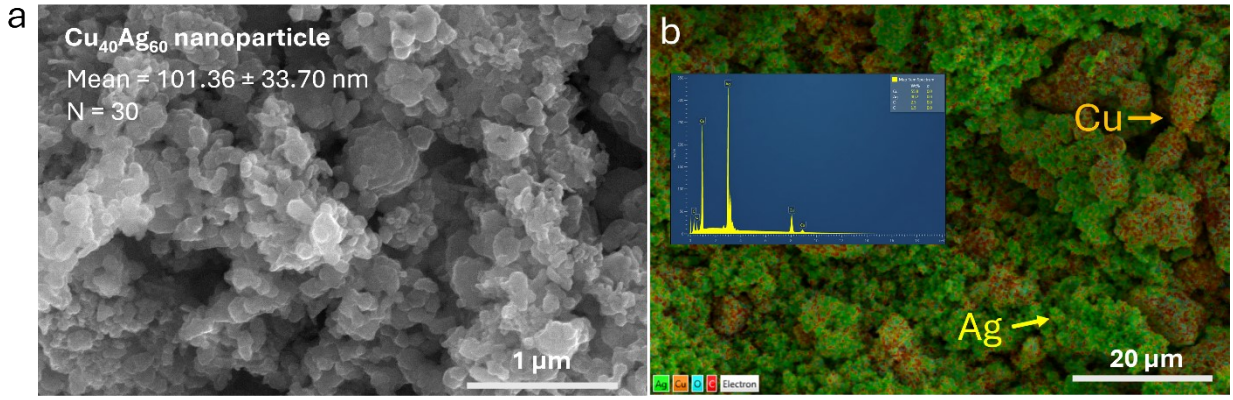

Figure S2 (a) SEM image and (b) corresponding EDS elemental mapping of $Cu_{40}Ag_{60}$ nanoparticle.

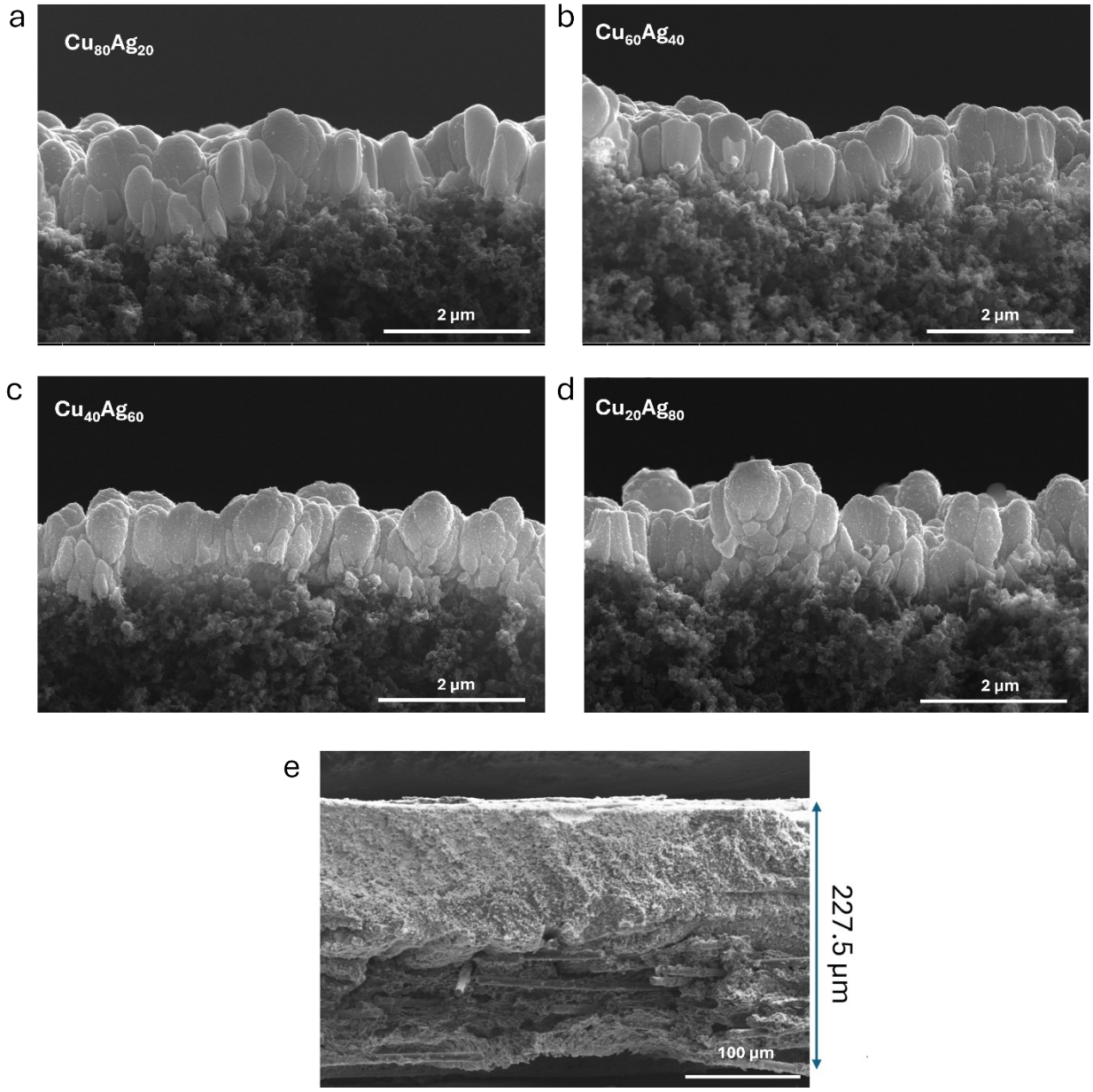

Figure S3 Cross-sectional SEM images of (a-d) the sputtered Cu-Ag catalysts, and (e) the entire GDE.

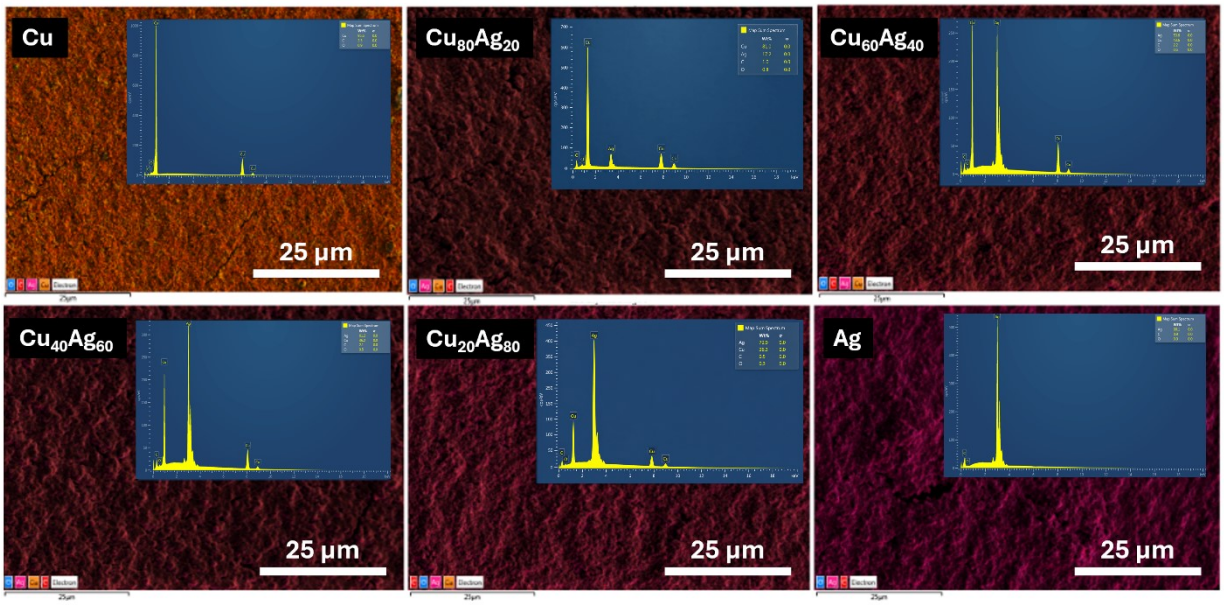

Figure S4 SEM-EDS images of Cu, $Cu_{80}Ag_{20}$, $Cu_{60}Ag_{40}$, $Cu_{40}Ag_{60}$, $Cu_{20}Ag_{80}$, and Ag catalysts, showing their surface morphologies and corresponding Cu:Ag elemental ratios as determined from EDS spectra.

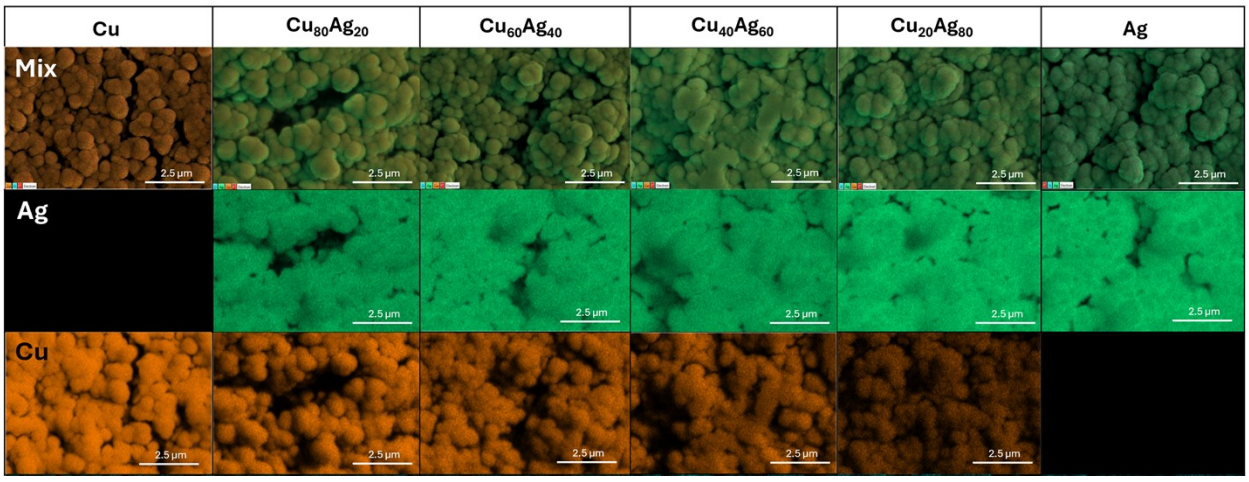

Figure S5 High-magnification SEM-EDS images of Cu, $Cu_{80}Ag_{20}$, $Cu_{60}Ag_{40}$, $Cu_{40}Ag_{60}$, $Cu_{20}Ag_{80}$, and Ag catalysts

Table S3 Atomic compositions of Cu, $Cu_{80}Ag_{20}$, $Cu_{60}Ag_{40}$, $Cu_{40}Ag_{60}$, $Cu_{20}Ag_{80}$, and Ag determined from SEM-EDS

Catalyst / Element	Cu	$Cu_{80}Ag_{20}$	$Cu_{60}Ag_{40}$	$Cu_{40}Ag_{60}$	$Cu_{20}Ag_{80}$	Ag
Cu (%atomic)	100	82.5±1.0	64.3±1.4	38.8±1.6	23.0±1.1	0
Ag (%atomic)	0	17.5±1.0	35.7±1.6	61.2±1.1	77±1.3	100

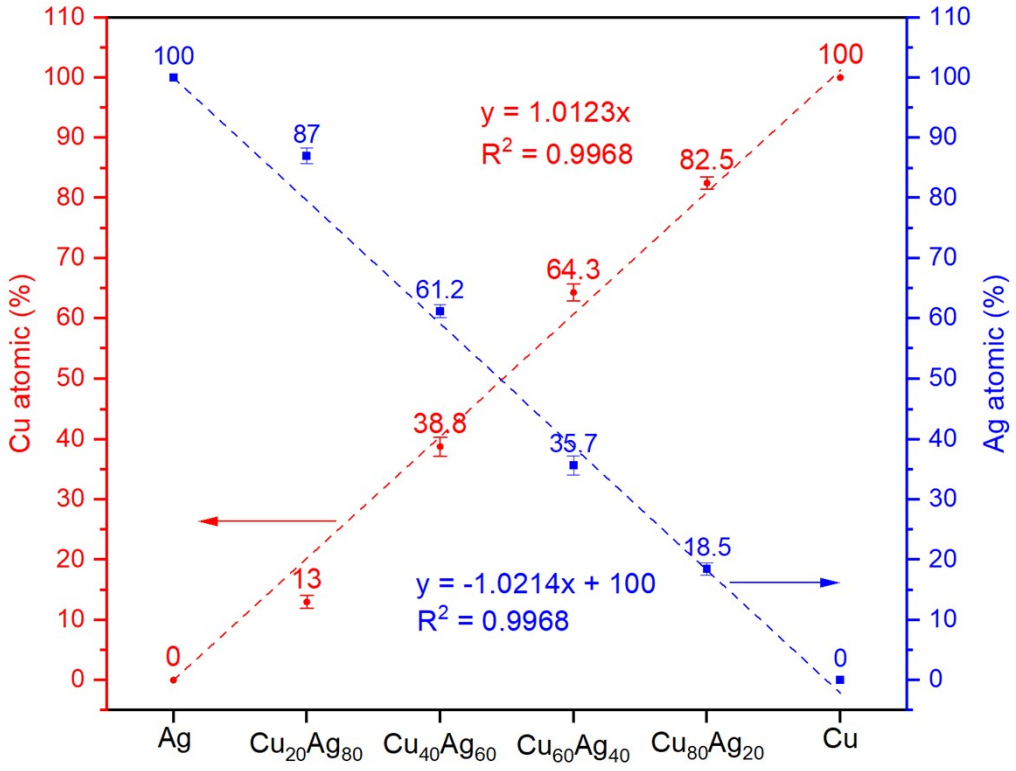

Figure S6 Atomic compositions of Cu, $Cu_{80}Ag_{20}$, $Cu_{60}Ag_{40}$, $Cu_{40}Ag_{60}$, $Cu_{20}Ag_{80}$, and Ag determined from SEM-EDS, showing a linear correlation between the nominal and measured compositions.

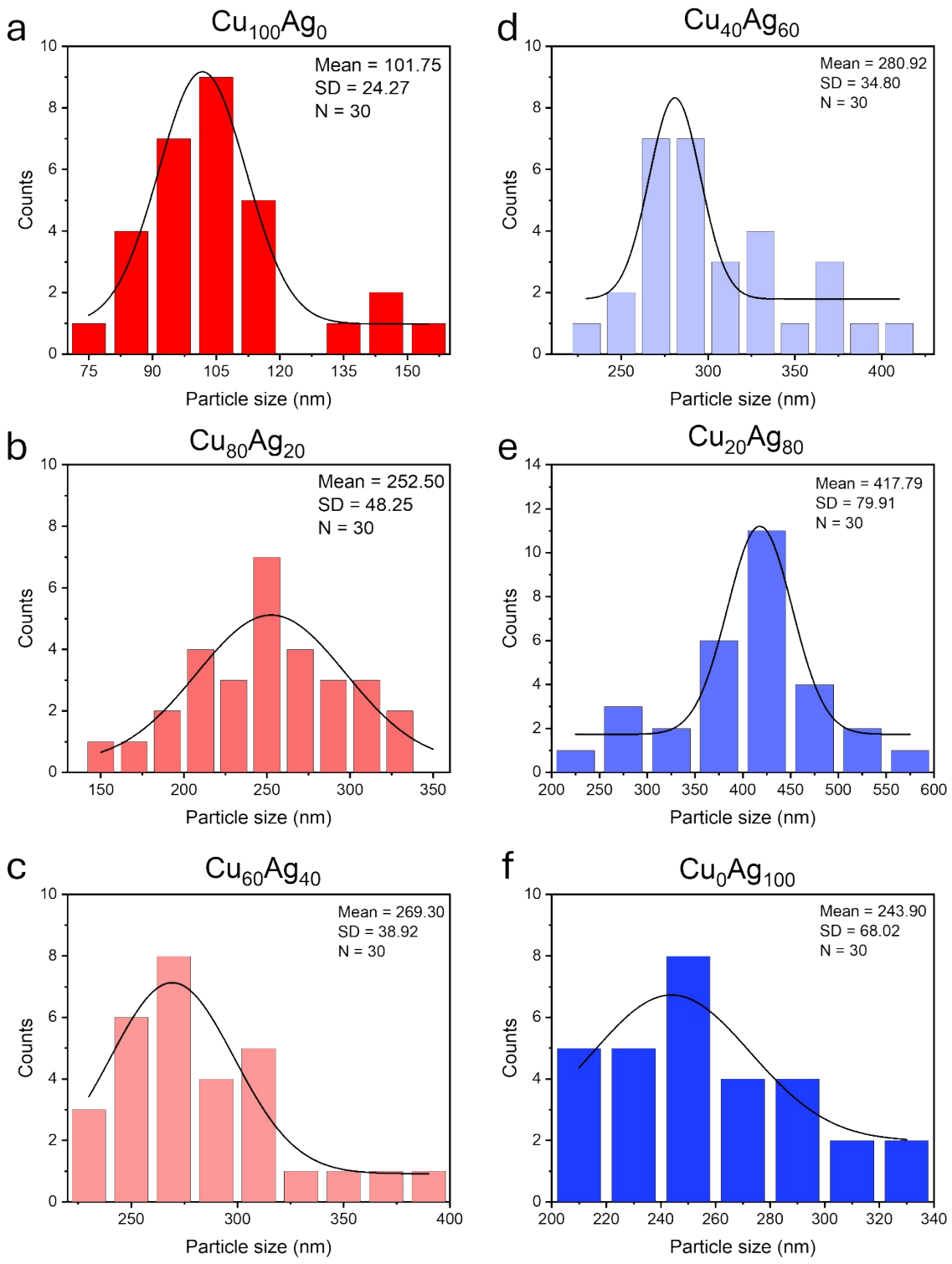

Figure S7 Particle size distribution of Cu, $Cu_{80}Ag_{20}$, $Cu_{60}Ag_{40}$, $Cu_{40}Ag_{60}$, $Cu_{20}Ag_{80}$, and Ag measured from Figure 1

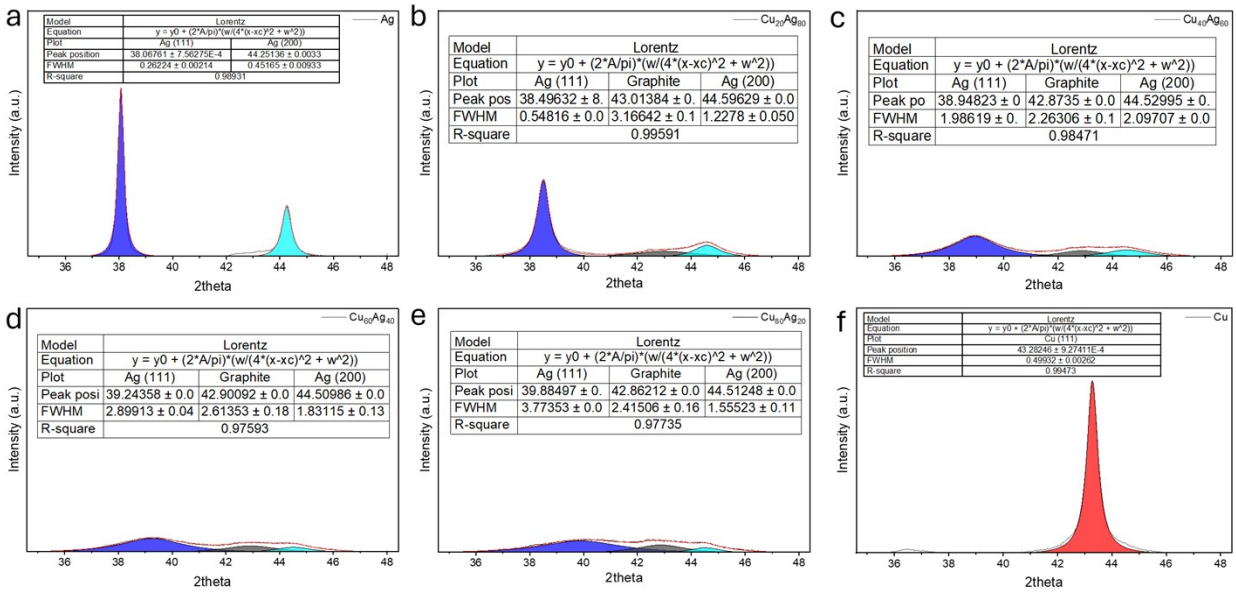

Figure S8 XRD peak deconvolution of the 2θ region of 36–46° for (a) Ag, (b) $Cu_{20}Ag_{80}$, (c) $Cu_{40}Ag_{60}$, (d) $Cu_{60}Ag_{40}$, (e) $Cu_{80}Ag_{20}$, and (f) Cu, resolving the overlapping contributions of Ag(111), Graphite, and Ag(200) reflections.

Table S4 Peak positions (2θ), FWHM, and crystallite sizes obtained from Lorentzian fitting of Cu, Ag, and Cu-Ag alloy reflections, together with graphite-related peaks, in the 2θ range of 36-46°.

Composition	**Peak**	**2θ (°)**	**FWHM (°)**	**Crystallite size D (nm)**
Cu	Cu(111)	43.28246	0.49932	17.12
$Cu_{80}Ag_{20}$	Graphite	42.86212	2.41506	3.53
	(111)	39.88497	3.77353	2.24
	(200)	44.51248	1.55523	5.52
$Cu_{60}Ag_{40}$	Graphite	42.90092	2.61353	3.27
	(111)	39.24358	2.89913	2.91
	(200)	44.50986	1.83115	4.69
$Cu_{40}Ag_{60}$	Graphite	42.87350	2.26306	3.77
	(111)	38.94823	1.98619	4.24
	(200)	44.52995	2.09707	4.09
$Cu_{20}Ag_{80}$	Graphite	43.01384	3.16642	2.70
	(111)	38.49632	0.54816	15.35
	(200)	44.59629	1.22780	6.99
Ag	Ag(111)	38.06761	0.26224	32.05
	Ag(200)	44.25136	0.45165	18.99

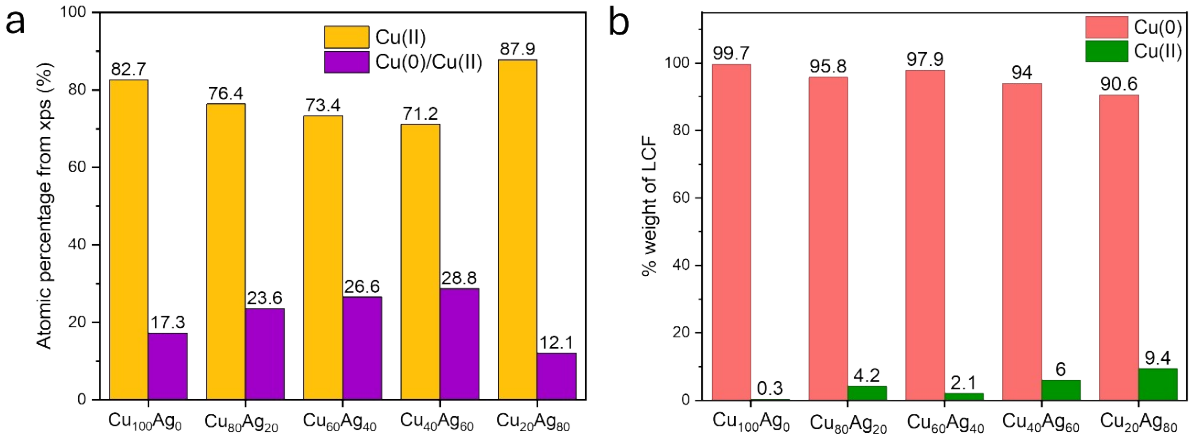

Figure S9 Cu oxidation states obtained from (a) XPS and (b) linear combination fitting of XANES spectra for $Cu_{100}Ag_0$, $Cu_{80}Ag_{20}$, $Cu_{60}Ag_{40}$, $Cu_{40}Ag_{60}$, and $Cu_{20}Ag_{80}$ catalyst.

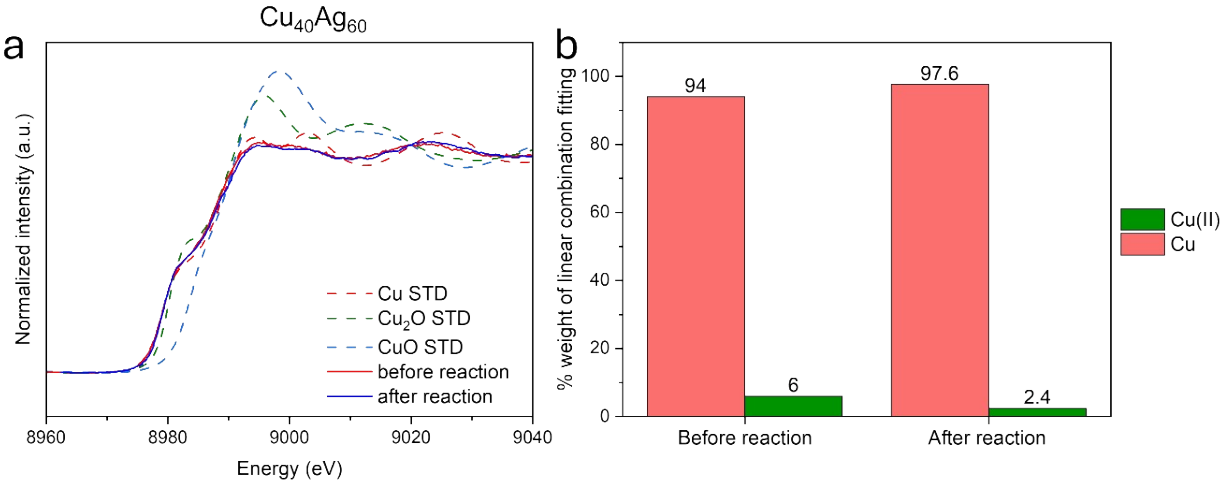

Figure S10 (a) Normalized Cu K-edge XANES spectra and (b) Cu oxidation states obtained from linear combination fitting of $Cu_{40}Ag_{60}$ spectra before and after reaction.

Table S5 EXAFS fitting parameters at the Cu K-edge for sputtered Cu-Ag catalysts.

Catalyst information	Path	CN	σ^2 (Å^{-2})	R (Å)	E_0
$Cu_{20}Ag_{80}$	Cu-Cu_1	6.02 ± 0.15	0.017 ± 0.002	2.51 ± 0.008	-0.95 ± 1.07
	Cu-Ag_1	2.01 ± 0.15	0.007 ± 0.001	2.66 ± 0.009	
	Cu-Cu_2	1.00 ± 0.15	0.007 ± 0.002	3.06 ± 0.023	
	Cu-Cu_3	2.01 ± 0.15	0.018 ± 0.009	4.03 ± 0.064	
$Cu_{40}Ag_{60}$	Cu-Cu_1	5.54 ± 0.12	0.011 ± 0.001	2.51 ± 0.008	1.05 ± 1.25
	Cu-Ag_1	1.85 ± 0.12	0.021 ± 0.004	2.68 ± 0.023	
	Cu-Cu_2	0.92 ± 0.12	0.009 ± 0.005	3.55 ± 0.046	
	Cu-Cu_3	1.85 ± 0.12	0.011 ± 0.004	4.01 ± 0.036	
$Cu_{60}Ag_{40}$	Cu-Cu_1	5.48 ± 0.14	0.001 ± 0.001	2.53 ± 0.011	4.20 ± 1.67
	Cu-Ag_1	1.83 ± 0.14	0.022 ± 0.007	2.77 ± 0.032	
	Cu-Cu_2	0.91 ± 0.14	0.007 ± 0.005	3.54 ± 0.043	
	Cu-Cu_3	1.83 ± 0.14	0.006 ± 0.003	4.03 ± 0.027	
$Cu_{80}Ag_{20}$	Cu-Cu_1	8.34 ± 0.15	0.014 ± 0.002	2.55 ± 0.011	3.98 ± 1.35
	Cu-Ag_1	1.67 ± 0.15	0.008 ± 0.002	2.68 ± 0.017	
	Cu-Cu_2	3.34 ± 0.15	0.015 ± 0.003	3.09 ± 0.025	
	Cu-Cu_3	1.67 ± 0.15	0.005 ± 0.003	4.05 ± 0.025	

Electrochemical testings

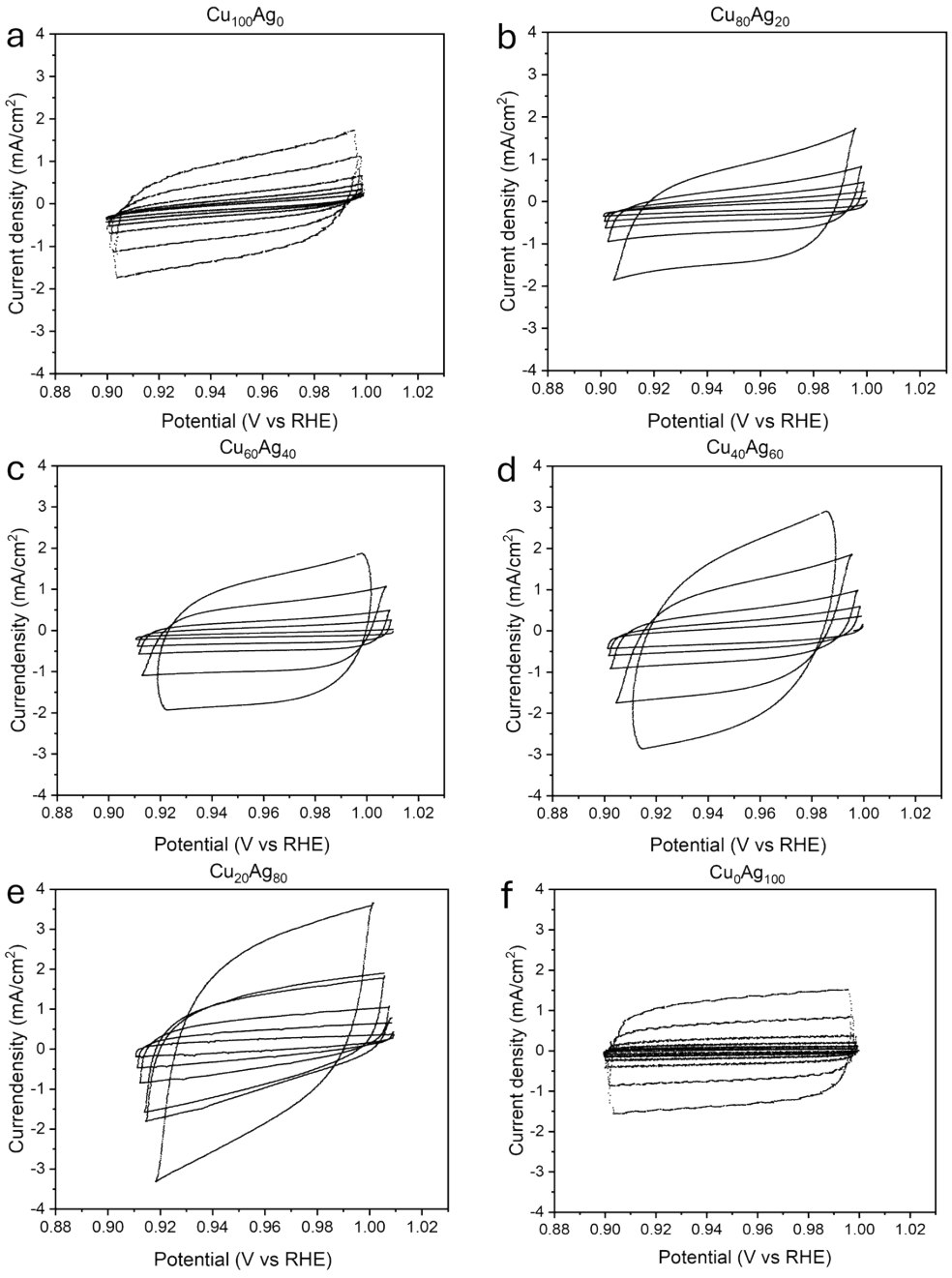

*

Figure S11 CV scans showing capacitive current measurements for (a) $Cu_{100}Ag_0$, (b) $Cu_{80}Ag_{20}$, (c) $Cu_{60}Ag_{40}$, (d) $Cu_{40}Ag_{60,}$ (e) $Cu_{20}Ag_{80,}$ and (f) $Cu_{100}Ag_0$ catalysts at scan rates from 5 to 100 mV s^{-1}

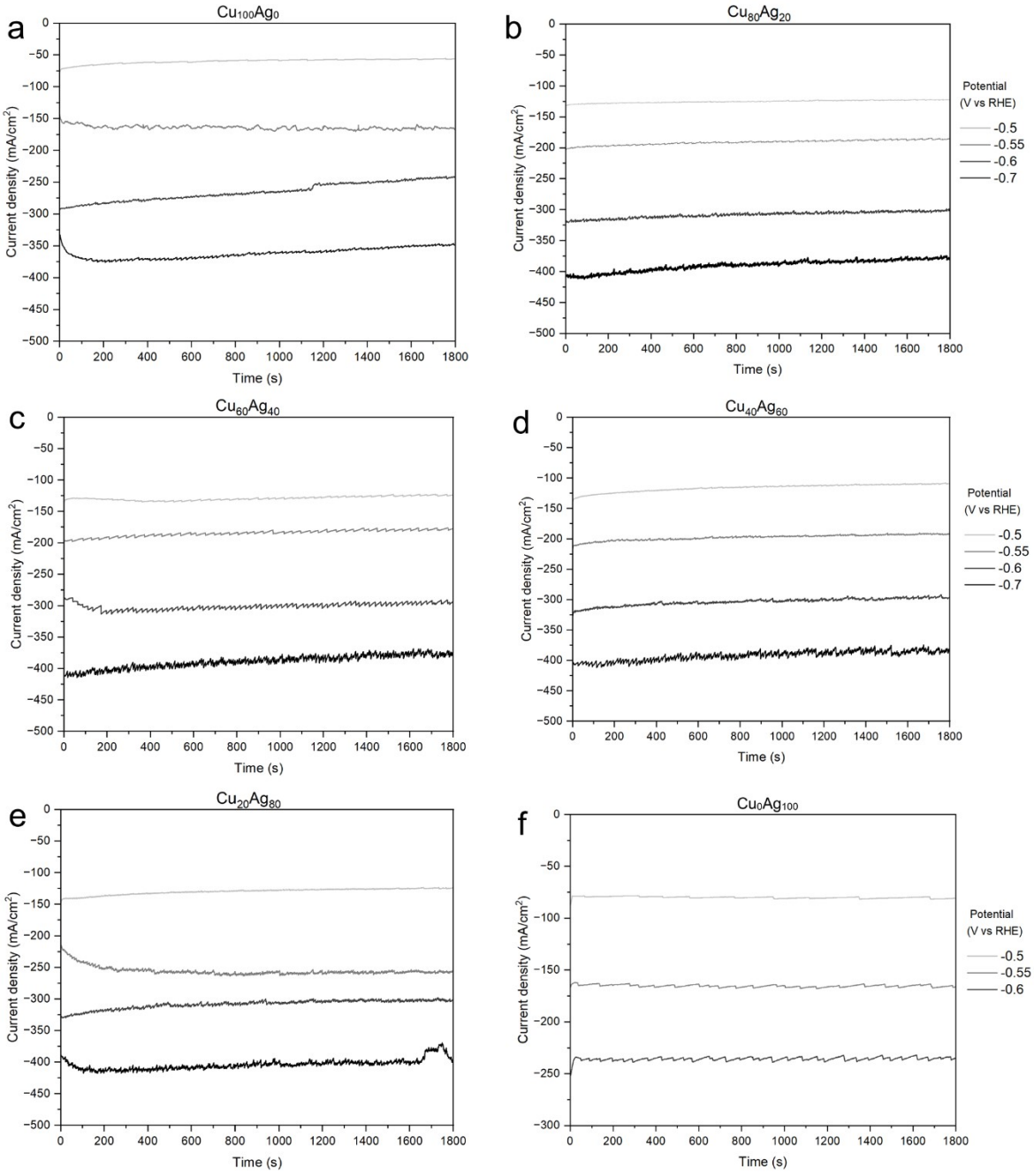

Figure S12 Current density profiles of Cu, $Cu_{80}Ag_{20}$, $Cu_{60}Ag_{40}$, $Cu_{40}Ag_{60}$ $Cu_{20}Ag_{80}$, and Ag catalysts measured at potentials of -0.5, -0.55, -0.6, and -0.7 V vs. RHE.

Table S6 Relative molar fraction of acetate in liquid products (FE/n).

Liquid product	$HCOO^-$	CH_3COO^-	EtOH	PrOH	mol% of acetate in liquid products
n	2	8	12	18	
$Cu_{100}Ag_0$	4.00	1.00	33.00	5.00	2.43
$Cu_{80}Ag_{20}$	5.10	14.30	28.40	1.50	26.34
$Cu_{60}Ag_{40}$	4.71	13.53	29.42	0.00	26.03
$Cu_{40}Ag_{60}$	3.68	31.12	9.09	0.00	59.99
$Cu_{20}Ag_{80}$	9.95	23.17	12.89	0.00	32.37

The mol% of acetate in the liquid products was calculated using the following equation:

$$\frac{\%FE_{acetate}/n_{acetate}}{\sum \%FE_i/n_i}$$

where i represents each liquid product and n is the number of electrons involved in the formation of the corresponding product.

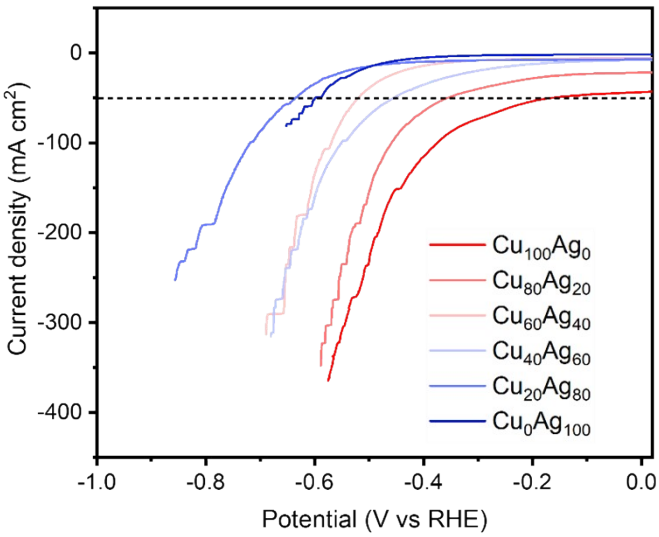

Figure S13 LSV profiles of Cu-Ag catalysts measured under N_2 atmosphere for HER activity evaluation.

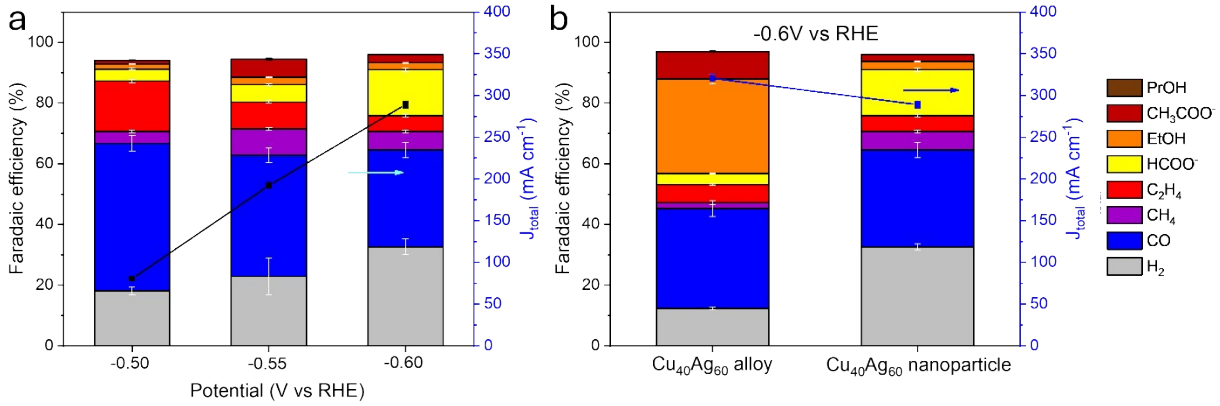

Figure S14 comparison of CO_2RR product distributions between Cu/Ag nanoparticles (Cu: Ag = 40:60 at%) and a sputtered $Cu_{40}Ag_{60}$ alloy catalyst at -0.60 V vs. RHE. **(b)** Potential-dependent CO_2RR product distributions of Cu/Ag nanoparticles measured at -0.50, -0.55, and -0.60 V vs. RHE.

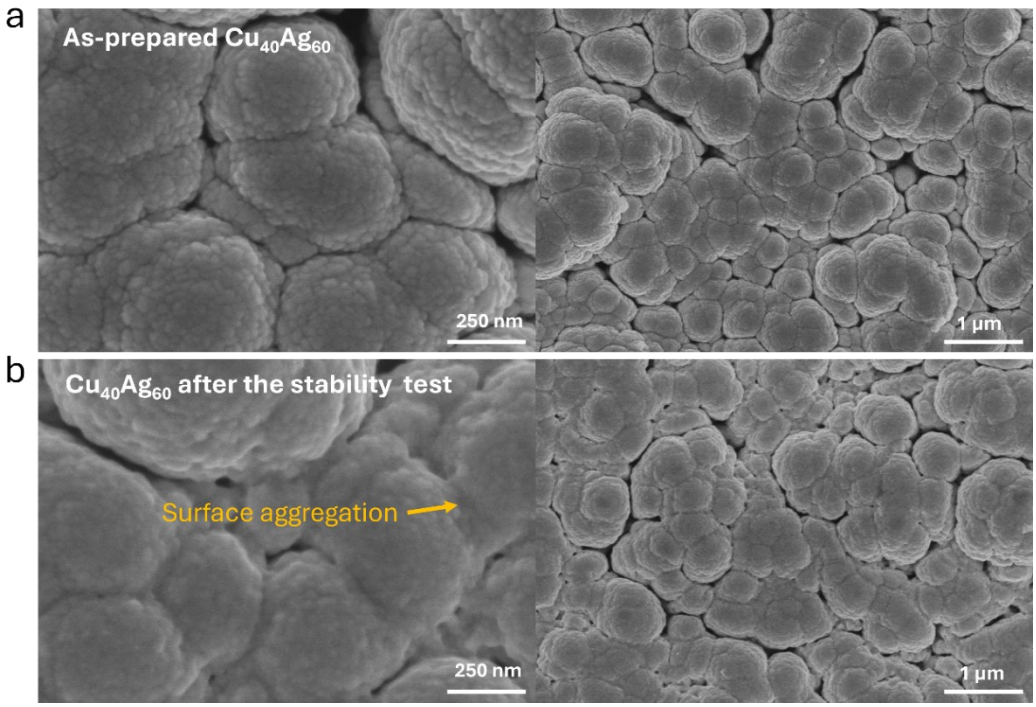

Figure S15 SEM images of (a) as-prepared $Cu_{40}Ag_{60}$ and (b) $Cu_{40}Ag_{60}$ after the stability test

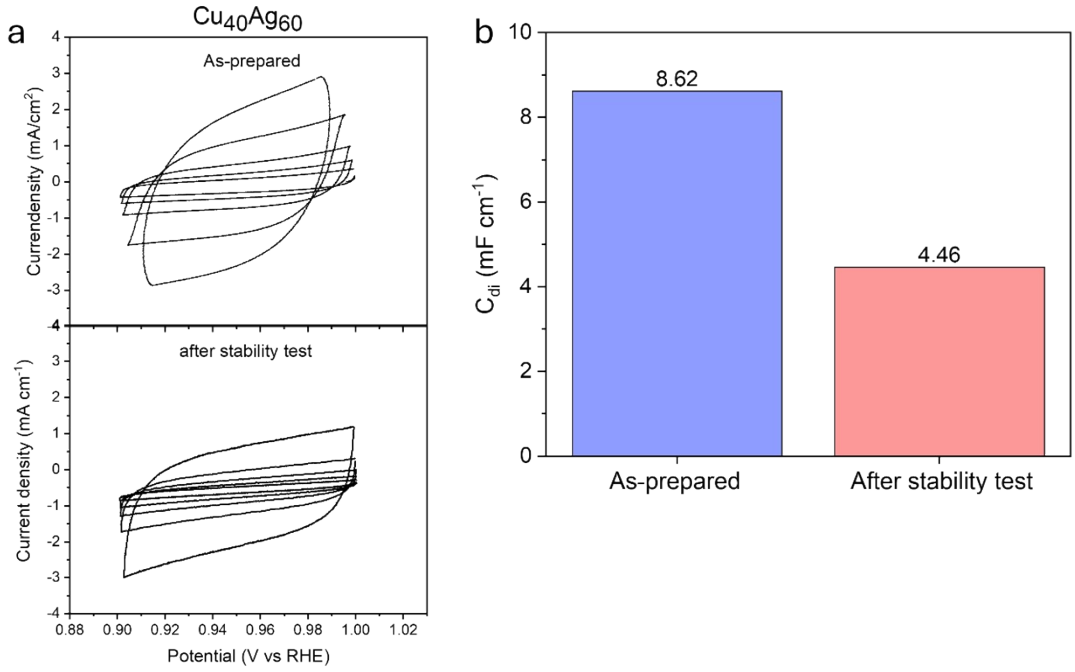

Figure S16 CV scans showing (a) capacitive current measurements for $Cu_{40}Ag_{60}$ before and after stability test and (b) double-layer capacitance (C_{dl}) values

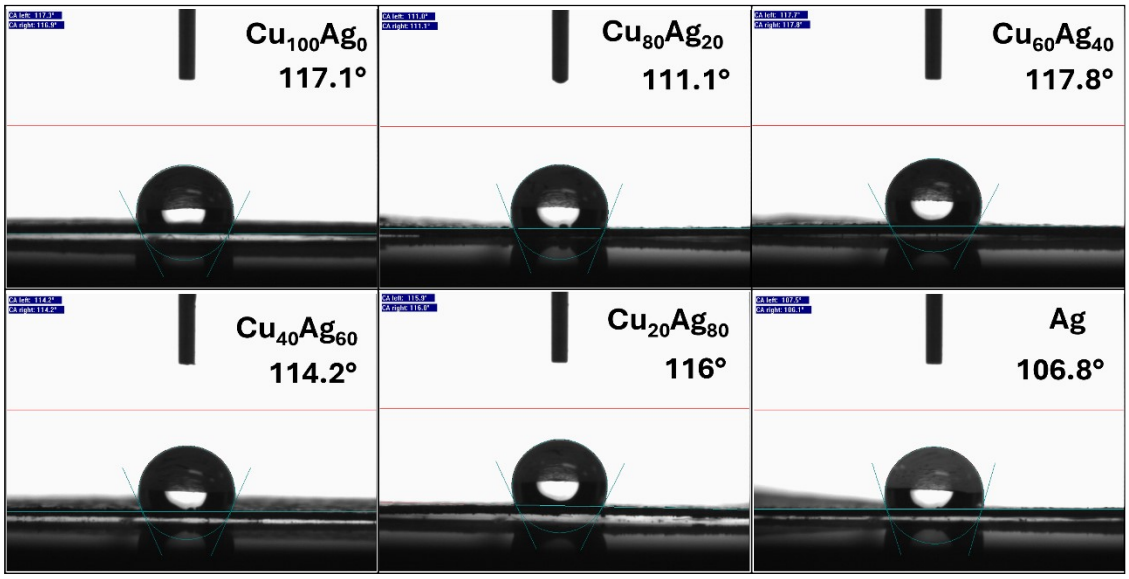

Figure S17 water contact angles of Cu, Ag and Cu-Ag alloy

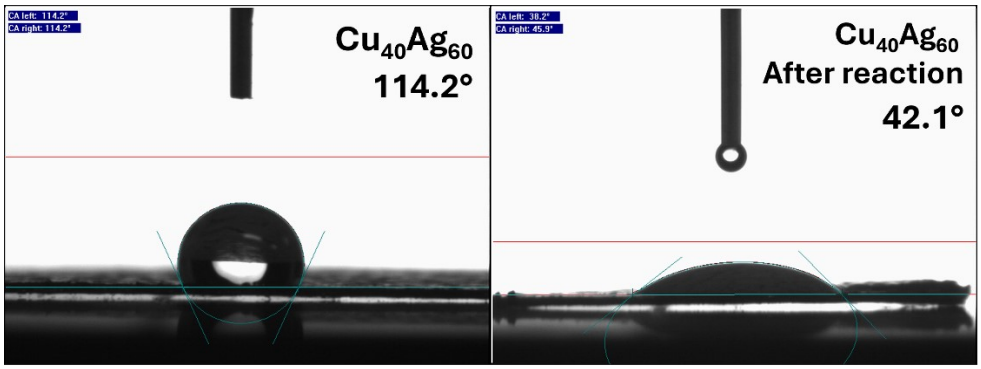

Figure S18 Water contact angles of $Cu_{40}Ag_{60}$ alloy before and after stability test.

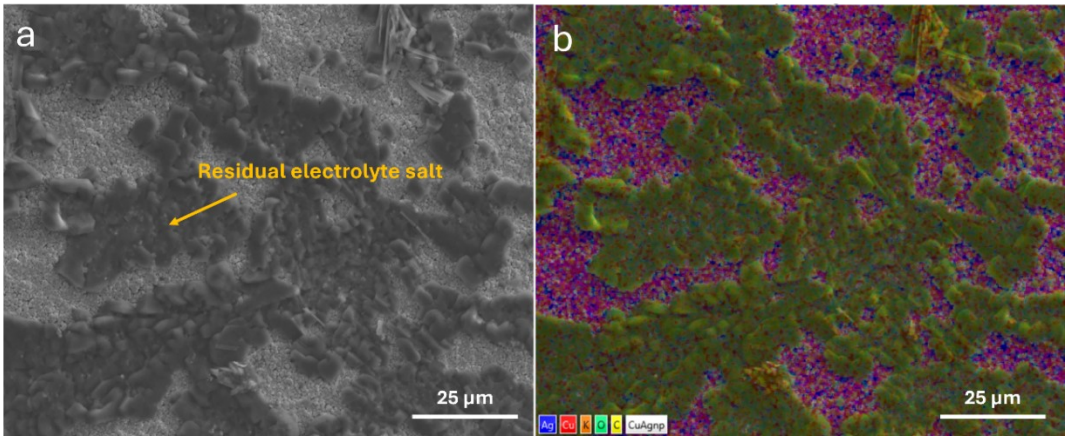

Figure S19 Post-reaction (a) SEM and (b) EDS mapping images of $Cu_{40}Ag_{60}$ after the stability test, showing residual electrolyte salt on the catalyst surface**.**

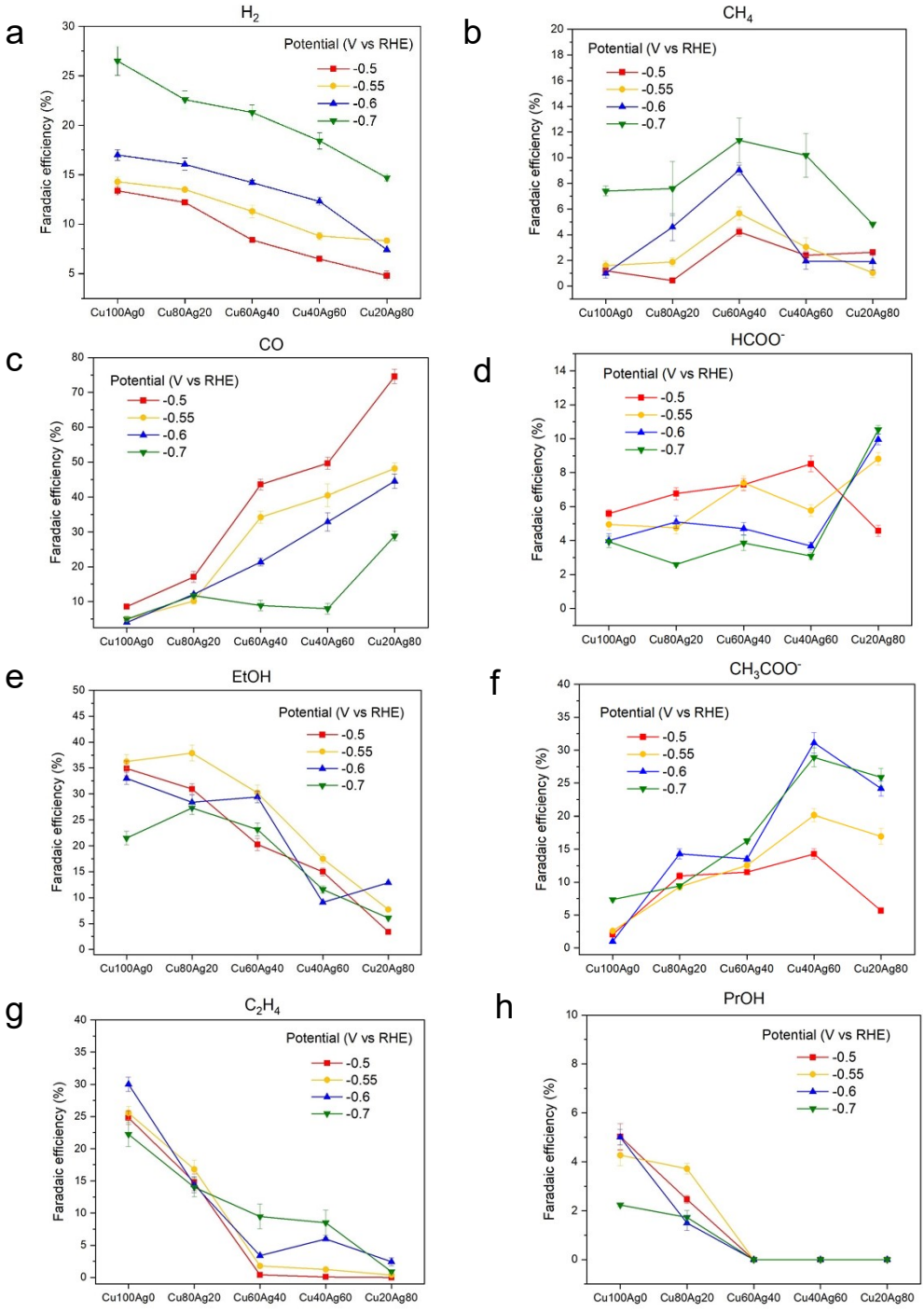

Figure S20 Faradaic efficiencies of major CO_2RR products over Cu, $Cu_{80}Ag_{20}$, $Cu_{60}Ag_{40}$, $Cu_{40}Ag_{60}$, and $Cu_{20}Ag_{80}$ catalysts at applied potentials of -0.5 V (red), -0.55 V (yellow), -0.6 V (purple), and -0.7 V (green) vs. RHE.

References

[1] M. Serafini, F. Mariani, A. Fasolini, E. Scavetta, F. Basile, D. Tonelli, Nanostructured copper-based electrodes electrochemically synthesized on a carbonaceous gas diffusion membrane with catalytic activity for the electroreduction of CO2, ACS applied materials & interfaces, 13 (2021) 57451-57461.
[2] Q. Zhu, X. Sun, D. Yang, J. Ma, X. Kang, L. Zheng, J. Zhang, Z. Wu, B. Han, Carbon dioxide electroreduction to C2 products over copper-cuprous oxide derived from electrosynthesized copper complex, Nature communications, 10 (2019) 3851.
[3] X.F. Qiu, J.R. Huang, C. Yu, Z.H. Zhao, H.L. Zhu, Z. Ke, P.Q. Liao, X.M. Chen, A stable and conductive covalent organic framework with isolated active sites for highly selective electroreduction of carbon dioxide to acetate, Angewandte Chemie, 134 (2022) e202206470.
[4] S. Gonglach, S. Paul, M. Haas, F. Pillwein, S.S. Sreejith, S. Barman, R. De, S. Müllegger, P. Gerschel, U.-P. Apfel, Molecular cobalt corrole complex for the heterogeneous electrocatalytic reduction of carbon dioxide, Nature communications, 10 (2019) 3864.
[5] Y. Liu, S. Chen, X. Quan, H. Yu, Efficient electrochemical reduction of carbon dioxide to acetate on nitrogen-doped nanodiamond, Journal of the American Chemical Society, 137 (2015) 11631-11636.
[6] H.-L. Zhu, H.-Y. Chen, Y.-X. Han, Z.-H. Zhao, P.-Q. Liao, X.-M. Chen, A porous π–π stacking framework with dicopper (I) sites and adjacent proton relays for electroreduction of CO2 to C2+ products, Journal of the American Chemical Society, 144 (2022) 13319-13326.
[7] Z. Cai, N. Cao, F. Zhang, X. Lv, K. Wang, Y. He, Y. Shi, H.B. Wu, P. Xie, Hierarchical Ag-Cu interfaces promote CC coupling in tandem CO2 electroreduction, Applied Catalysis B: Environmental, 325 (2023) 122310.
[8] L.R.L. Ting, O. Pique, S.Y. Lim, M. Tanhaei, F. Calle-Vallejo, B.S. Yeo, Enhancing CO2 electroreduction to ethanol on copper–silver composites by opening an alternative catalytic pathway, ACS catalysis, 10 (2020) 4059-4069.
[9] Y. Yu, D. Wang, Y. Hong, T. Zhang, C. Liu, J. Chen, G. Qin, S. Li, Bulk-immiscible CuAg alloy nanorods prepared by phase transition from oxides for electrochemical CO 2 reduction, Chemical Communications, 58 (2022) 11163-11166.
[10] C. Chen, Y. Li, S. Yu, S. Louisia, J. Jin, M. Li, M.B. Ross, P. Yang, Cu-Ag tandem catalysts for high-rate CO2 electrolysis toward multicarbons, Joule, 4 (2020) 1688-1699.
[11] P. Iyengar, M.J. Kolb, J.R. Pankhurst, F. Calle-Vallejo, R. Buonsanti, Elucidating the facet-dependent selectivity for CO2 electroreduction to ethanol of Cu–Ag tandem catalysts, Acs Catalysis, 11 (2021) 4456-4463.
[12] X. Lv, L. Shang, S. Zhou, S. Li, Y. Wang, Z. Wang, T.K. Sham, C. Peng, G. Zheng, Electron-deficient Cu sites on Cu3Ag1 catalyst promoting CO2 electroreduction to alcohols, Advanced Energy Materials, 10 (2020) 2001987.
[13] Z. Feng, C. Hu, H. Tang, K. Shen, L. Chen, Y. Li, Dual-atomic Cu–Ag pairs boosting selective electroreduction of CO 2 to acetate, Chemical Science, 16 (2025) 9385-9392.
[14] C. Choi, J. Cai, C. Lee, H.M. Lee, M. Xu, Y. Huang, Intimate atomic Cu-Ag interfaces for high CO2RR selectivity towards CH4 at low over potential, Nano Research, 14 (2021) 3497-3501.
[15] D. Wei, Y. Wang, C.L. Dong, Z. Zhang, X. Wang, Y.C. Huang, Y. Shi, X. Zhao, J. Wang, R. Long, Decrypting the controlled product selectivity over Ag− Cu bimetallic surface alloys for electrochemical CO2 reduction, Angewandte Chemie, 135 (2023) e202217369.
[16] Y.C. Li, Z. Wang, T. Yuan, D.-H. Nam, M. Luo, J. Wicks, B. Chen, J. Li, F. Li, F.P.G. De Arquer, Binding site diversity promotes CO2 electroreduction to ethanol, Journal of the American Chemical Society, 141 (2019) 8584-8591.

[17] M.L. Frisch, L. Wu, C. Atlan, Z. Ren, M. Han, R. Tucoulou, L. Liang, J. Lu, A. Guo, H.N. Nong, Unraveling the synergistic effects of Cu-Ag tandem catalysts during electrochemical CO2 reduction using nanofocused X-ray probes, Nature Communications, 14 (2023) 7833.
[18] Y. Xu, C. Li, Y. Xiao, C. Wu, Y. Li, Y. Li, J. Han, Q. Liu, J. He, Tuning the selectivity of liquid products of CO2RR by Cu–Ag alloying, ACS Applied Materials & Interfaces, 14 (2022) 11567-11574.
[19] S. Zhang, B. Zhang, S. Yang, T. Shao, X. Li, R. Cao, M. Cao, Nanoscale Cu–Ag Heterostructures for CO2 Reduction to C2+ Products, ACS Applied Nano Materials, (2025).
[20] Y. Zhong, X. Kong, Z. Song, Y. Liu, L. Peng, L. Zhang, X. Luo, J. Zeng, Z. Geng, Adjusting local CO confinement in porous-shell Ag@ Cu catalysts for enhancing C–C coupling toward CO2 eletroreduction, Nano Letters, 22 (2022) 2554-2560.